Extended Short-Wave Photodiode based on CdSe/HgTe/Ag2Te Stack with High Internal Efficiency

Prachi Rastogi, Eva Izquierdo, Charlie Gréboval, Mariarosa Cavallo, Audrey Chu, Tung Huu Dang, Adrien Khalili, Claire Abadie, Rodolphe Alchaar, Stefano Pierini, et al.

Extended Short-Wave Photodiode based on CdSe/HgTe/Ag_2Te Stack with High Internal Efficiency

Prachi Rastogi[1], Eva Izquierdo[1], Charlie Gréboval[1], Mariarosa Cavallo[1], Audrey Chu[1], Tung Huu Dang[1], Adrien Khalili[1], Claire Abadie[1], Rodolphe Alchaar[1], Stefano Pierini[1], Herve Cruguel[1], Nadine Witkowski[1], James K. Utterback[1], Thibault Brule[2], Xiang Zhen Xu[3], Philippe Hollander[4], Abdelkarim Ouerghi[5], Bruno Gallas[1], Mathieu G. Silly[4], Emmanuel Lhuillier[1*]

[1] Sorbonne Université, CNRS, Institut des NanoSciences de Paris, INSP, F-75005 Paris, France.
[2]HORIBA Scientific, HORIBA France S.A.S, Avenue de la Vauve, Passage Jobin Yvon, 91120 Palaiseau, France
[3] Laboratoire de Physique et d'Etude des Matériaux, ESPCI-Paris, PSL Research University, Sorbonne Université Univ Paris 06, CNRS UMR 8213, 10 rue Vauquelin 75005 Paris, France.
[4]Synchrotron-SOLEIL, Saint-Aubin, BP48, F91192 Gif sur Yvette Cedex, France.
[5]Centre de Nanosciences et de Nanotechnologies, CNRS, Univ. Paris-Sud, Université Paris-Saclay, 10 Boulevard Thomas Gobert, 91120 Palaiseau, France

Abstract: Nanocrystal integration into focal plane arrays requires the development of new photodiode designs combining an efficient charge dissociation with a low dark current. Previously reported architectures based on HgTe/Ag_2Te stacks appear to be sub-optimal for cut-off wavelengths below 2.5 µm. Here, we show that the introduction of a thin and strongly coupled CdSe layer acting as an electron transport layer and a unipolar barrier drastically improves the electrical performances. This diode achieves a responsivity as high as 0.8 $A \cdot W^{-1}$, corresponding to an internal efficiency above 90 % for a 2 µm cut-off wavelength. The specific detectivity is close to 10^{11} Jones at room temperature and reaches 9×10^{11} Jones at 200 K, the highest value reported for HgTe nanocrystal-based photodiode with operation around 2 µm. The diode time response can be as short as 200 ns and appears to be limited by band bending dynamics as revealed by time-resolved photoemission measurements.

Keywords: short wave infrared, detection, HgTe, nanocrystals, time resolved photoemission.

*To whom correspondence should be sent: el@insp.upmc.fr

INTRODUCTION

HgTe nanocrystals (NCs)[1] have a broadly tunable absorption spectrum in the infrared (IR) range. They have become a viable building block for the design of IR optoelectronic devices, ranging from light-emitting diodes[2,3] to light sensors. Many device geometries have been explored for the latter application, from photoconductors[4] to photodiodes,[5] including gate-controlled phototransistors.[6–8] Among the main developments, it is worth mentioning their integration into the focal plane arrays,[9,10] design of multicolor sensors,[11] coupling to light resonators to shape[12–14] the absorption spectrum or nano-sized devices[15] to take benefit of the local strong interparticle coupling.[16]

So far, vertical geometry has led to the best performances. The in-built electric field of the device enables a zero-bias operation and consequently a reduction in dark current and noise spectral density. While for PbS NCs, near-unity efficiency diodes are now established, this still has to be demonstrated for HgTe. The shift of the spectral response toward longer wavelengths compared to PbS requires a complete update of the band structure to achieve a suitable band alignment. Several concepts have been explored, such as introducing unipolar barriers[17] or gate tunable carrier extraction.[18] To date, the most efficient diode structure is based on a HgTe absorbing layer coupled to Ag_2Te used as a hole transport layer [5] (HTL). While using this HTL leads to high performance, several open questions still have to be addressed, such as the nature of the coupling between the HgTe and Ag_2Te layers. More importantly, this HTL layer was initially designed for HgTe NCs absorbing layer in the mid-wave infrared[5] (MWIR corresponding 5 µm cut-off wavelength) and only later shifted to the extended short wave infrared [19] (e-SWIR: 2.5 µm cut-off wavelength). It will be highly desirable to apply the same concept to even shorter wavelengths (1.8 or 2 µm cut-off wavelength) to directly compete with the InGaAs technology. However, it has recently been proven that the HgTe/Ag_2Te stack presents a reduced performance when cut-off wavelengths below 2.5 µm are targeted,[19] although fewer thermally activated carriers should be generated as the band gap is increased. This drop in performance can be directly connected to the doping cross-over of HgTe NCs. Large HgTe NCs, with MWIR absorption, have an *n*-type nature. The material shifts to an ambipolar nature around 2.5 µm and finally to a *p*-type character for strongly confined (small) NCs.[17] Consequently, the HgTe/Ag_2Te stack, which forms a *p*-*n* junction in the MWIR, corresponds only to a pp' junction in the SWIR, where the current rectification now results from Schottky contacts. Thus, there is a need to introduce an *n*-type electron transport layer (ETL) to achieve efficient charge dissociation when using 1.8-2 µm cut-off wavelength HgTe NCs. Here, we demonstrate that such a *n*-type layer can be obtained from a thin layer of large CdSe nanocrystals. The obtained stack based on CdSe/HgTe/Ag_2Te is then used to design a 2 µm cut-off wavelength photodiode with responsivity up to 0.8 $A \cdot W^{-1}$ corresponding to above 90% internal quantum efficiency. The specific detectivity reaches almost 10^{11} Jones at room temperature and 10^{12} Jones at 200 K, making this device match not only state-of-the-art HgTe NC-based devices but also available commercial technologies.[1,20] The time response appears to be in the 200-700 ns range depending on the pixel size, and we demonstrate using time-resolved photoemission that this time response can be directly connected to the carrier dielectric relaxation. Finally, we discuss where future efforts should be focused to push the external quantum efficiency (EQE) close to 100%.

METHODS

Chemicals: Mercury chloride ($HgCl_2$, Sigma-Aldrich, 99%), **Mercury compounds are highly toxic. Handle them with special care.** tellurium powder (Te, Sigma-Aldrich, 99.99%), selenium powder (Alfa Aesar, 99 %), cadmium oxide (Alfa Aesar, 99.95 %), silver nitrate (Alfa Aesar, 99.9 %), sodium sulfide hydrate (Alfa Aesar, flake), myristic acid (Fluka, > 98 %), trioctylphosphine (TOP, Alfa Aesar, 90%), Octadecene (ODE, Acros Organics, 90%), oleic acid (OA, Sigma, 90%), oleylamine (OLA, Acros, 80-90%), dodecanethiol (DDT, Sigma-Aldrich, 98%), 1,2 ethanedithiol (EDT, Fluka, 98%), Hydrochloric acid (HCl, Mieuxa, 25%), ethanol absolute anhydrous (VWR), methanol (VWR, >98%), isopropanol (IPA, VWR), hexane (VWR, 99%), octane (Carlo erba, 99%), 2-mercaptoethanol

(MPOH, Merck, >99%), N,N dimethylformamide (DMF, VWR), N-methylformamide (NMF, Alfa Aesar, 99%), chlorobenzene (VWR), toluene (VWR, 99.8 %). All chemicals are used without further purification except oleylamine that is centrifuged before use.

1 M TOP:Te precursor: 2.54 g of Te powder is mixed in 20 mL of TOP in a three neck flask. The flask is kept under vacuum at room temperature for 5 min and then the temperature is raised to 100 °C. Furthermore, degassing of flask is conducted for the next 20 min. The atmosphere is switched to nitrogen and the temperature is raised to 275 °C. The solution is stirred until a clear orange coloration is obtained. The flask is cooled down to room temperature and the color changes to yellow. Finally, this solution is transferred to a nitrogen filled glove box for storage.

0.1 M Se-ODE precursor: In a 100 mL three neck flask, 46.7 mL of ODE are degassed at room temperature for 30 min. Meanwhile, a suspension of 393 mg of Se in 3 mL of ODE is prepared. After degassing, the atmosphere is switched to nitrogen and the temperature is raised to 170 °C. The suspension is added portion wise (300 µL), waiting between each addition for the complete dissolution of the Se. Once all the Se is completely dissolved in the ODE, the solution is heated 1h at 215 °C. The solution turns orange-red to yellow. The flask is cooled down to room temperature. The solution is transferred in glove box.

Cadmium myristate precursor: In a 100 mL three neck flask, 2.56 g of CdO and 11 g of myristic acid are degassed under vacuum for 30 minutes at 70°C. Under argon flow, the mixture is heated up to 200 °C for 30 minutes until the solution becomes colorless. Then, 50 mL of MeOH is added between 60 °C and 70 °C to solubilize the excess of myristic acid. The mixture is stirred for 30 minutes. At the end, the cadmium myristate is precipitated by using centrifuge tube through the addition of MeOH. The washing procedure is repeated at least three times. The cadmium myristate is dried overnight under vacuum.

Cadmium oleate (0.5 M) precursor: 0.5 M cadmium oleate solution is synthesized by heating 10 mmol of cadmium oxide in 20 mL of oleic acid at 160 °C under N_2 until a colorless solution is obtained. The solution is then degassed under vacuum at 100 °C for 1 h.

HgTe NCs synthesis with band-edge at 6000 cm^{-1}: In a 50 mL three-neck flask, 540 mg of $HgCl_2$ and 50 mL of oleylamine are degassed under vacuum at 110 °C. At this stage, the solution is yellow and clear. Meanwhile, 2 mL of TOP:Te (1 M) is extracted from the glove box and is mixed with 8 mL of oleylamine. The atmosphere is switched to N_2 and the temperature is set at 57 °C. The pre-heated TOP:Te solution is quickly injected and the solution turns dark after 1 min. After 3 min, 10 mL of a mixture of 20% DDT in toluene is injected and a water bath is used to quickly decrease the temperature. The content of the flask is spilt in 4 tubes and MeOH is added. After centrifugation, the formed pellets are redispersed in one centrifuge tube with 10 mL of toluene. The solution is precipitated a second time with absolute EtOH. Again, the formed pellet is redispersed in 8 mL of toluene. At this step, the CQDs are centrifuged in pure toluene to remove the lamellar phase. The solid phase is discarded and the supernatant filtrated.

Ag_2Te CQD synthesis: In a 25 mL three neck flask, 34 mg $AgNO_3$ (0.2 mM), 5 mL OLA and 0.5 mL OA are degassed at 70 °C under vacuum until the $AgNO_3$ is completely dissolved and the solution becomes clear. Under nitrogen, 0.5 mL TOP is injected into the solution. Then the temperature is raised to 160 °C. At 160 °C the solution becomes orange. Then, 0.1 mL TOPTe (1 M) is injected into the solution and the reaction is quenched after 10 min with a water bath. The CQDs are precipitated with methanol and redispersed in chlorobenzene. At this step, 500 µL of DDT are added. The washing step is repeated one more time and finally the CQDs are redispersed in hexane:octane (9:1) solution.

CdSe NCs synthesis: In a 100 mL three neck flask, 170 mg of $Cd(myr)_2$ and 7.5 mL of ODE are degassed at room temperature for 30 min. Then, the reaction is put under nitrogen and heated up at 250 °C. Meanwhile, a suspension of Se (24 mg) in 2 mL of ODE is prepared. At 250°C, 1 mL of this solution is rapidly injected (suspension is sonicated just before the injection). Immediately after the injection, the temperature controller is set at 240°C and the reaction is heated for 5 min. After this time, 200 µL of oleic acid are added and the temperature controller is set at 260°C. At 260°C, 2 mL of oleylamine are added and the reaction is heated for 10 min. Meanwhile, 2 mL of $Cd(OA)_2$ 0.5 M and 10 mL of Se-ODE 0.1 M are mixed. 11 mL of the previous mixture is injected with a flow rate of 10 mL/h. Then, the reaction is left cooling down to room temperature. The reaction mixture is split into two centrifuge tubes and the round-bottomed flask is rinsed with 10 mL of hexane which are distributed over the two centrifuge tubes. The particles are precipitated by adding 30 mL of EtOH in each centrifuge tube. The mixtures are centrifuged at 6000 rpm for 10 min. The supernatants are discarded and both pellets (containing mainly the CdSe cores) are assembled into 10 mL of hexane. The CdSe cores are precipitated with 40 mL of EtOH. The mixture is centrifuged at 5500 rpm for 10 min. The supernatant is discarded and the pellet is dispersed into 10 mL of hexane.

CdSe ink: 800 µL of Na_2S solution in NMF (0.1 M) are added to 400 µL of CdSe solution and mixed with vortex and sonication. After a few seconds, two phases are observed. The apolar phase is removed and the polar phase is cleaned three times with hexane. The nanoparticles are precipitated by adding toluene and centrifuged at 6000 rpm for 2 min. Supernatant is discarded and the QDs are redispersed with 100 µL of DMF. A second centrifugation is performed with toluene. Finally, the QDs are redispersed with 100 µL of DMF.

HgTe ink*:* 1 mL of HgTe CQD solution in toluene is mixed with 1 mL of exchange solution as previously reported.[21] 5 mL of hexane is added to the solution and mixed with vortex and sonication. After a few seconds, two phases are clearly visible and the hexane one is removed. The solution is cleaned with hexane one more time. At this step, 250 µL of DMF is added to avoid precipitation. The solution is cleaned again with hexane. Then, the solution is precipitated by adding ethanol and centrifuged at 6000 rpm for 4 min. Supernatant is discarded and the QDs are redispersed in 130 µL of DMF.

Diode fabrication: For the device fabrication, 70 nm FTO ($\rho_s \approx 70$-90 Ω/sq) on glass substrate from Solems are used. To define the electrode area, FTO electrodes are patterned with optical UV lithography. The FTO-coated glass substrates are sequentially cleaned in acetone and isopropanol. The substrates are exposed to UV-ozone for 5 min. The CdSe ink is deposited onto the patterned FTO substrate via spin-coating (800 rpm for 2 min). The CdSe film is annealed on a hot plate at 200 °C for 20 min. The HgTe CQD ink (band edge at 6000 cm^{-1}) is deposited onto the CdSe film via spin-coating. The thickness of the film is tuned with spin-coating speed and ink concentration in DMF solvent. On top of HgTe ink film Ag_2Te CQDs layer is spin-coated at 2000 rpm followed by $HgCl_2$ treatment. For $HgCl_2$ treatment, 50 µL of $HgCl_2$ methanol (10 mM) solution is dropped onto HgTe film and spin-dried after 15 s. Then the film is rinsed with IPA. This procedure is repeated twice. Finally, an EDT ligand-exchange is performed by dipping the film in 1% EDT acetonitrile solution for 30 s and rinsed with pure acetonitrile. An 80 nm Au top electrode is deposited by thermal evaporation under a vacuum of $\approx 5 \times 10^{-6}$ mbar at the rate of 3 Å/s. The thickness is monitored with *in situ* quartz crystals. The substrate holder is rotated during the deposition to ensure homogeneous thickness. The overlap area of both electrodes FTO and Au is defined as the device area of 1 mm^2.

DISCUSSION AND RESULTS

To better understand the need for an ETL layer while designing a SWIR photodiode based on HgTe NCs, we fabricate a diode based on a simple HgTe/Ag_2Te stack,[11–13,22] see **Figure 1**b. The HgTe NCs are grown using the procedure developed by Keuleyan *et al*.[23] The NCs (Figure S1) present an exciton above 6000 cm^{-1} (*i.e.,* 1.7 µm) in solution leading to a cut-off wavelength at 5000 cm^{-1} (*i.e.,* 2 µm) on film due to a spectral shift induced by the NC coupling and change of surrounding dielectric constant, see **Figure 1**a. Field-effect measurements conducted in an electrolyte-gated transistor configuration show an ambipolar nature for HgTe NCs with clear prevailing hole conduction (*i.e.,* higher conductance under negative gate bias, **Figure 1**c). As expected,[5] the Ag_2Te NCs (Figure S2) present only p-type conduction, see **Figure 1**d. Consequently, the HgTe/Ag_2Te stack (completed with fluorine-doped tin oxide and gold contact) presents poorly rectifying I-V curves under dark condition, see **Figure 1**e. Under illumination, the curve nonetheless presents an apparent open-circuit voltage.

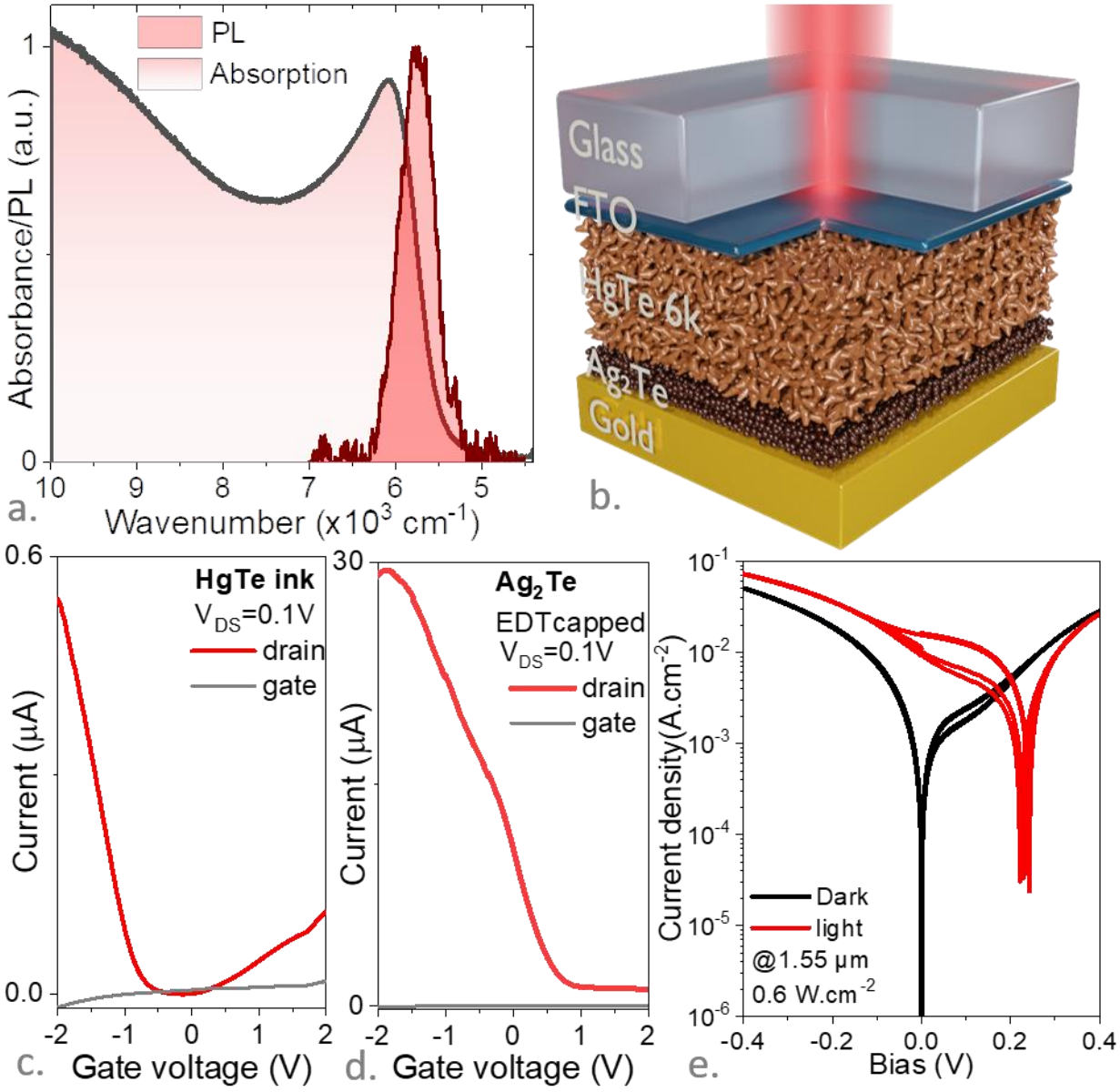

Figure 1 *a. Absorption and photoluminescence spectra of HgTe NCs. b. Schematic of HgTe/Hg:Ag_2Te photodiode used for SWIR light sensing. c. (resp d.) Transfer curves (drain and gate currents as a function of applied gate bias, under constant drain source bias; set here at 0.1 V) for an electrolyte-gated FET whose channel is made of HgTe (resp. Ag_2Te) NCs. e. I-V curves for the photodiode depicted in part b under dark condition and under illumination by a 1.55 µm laser diode delivering a 0.6 $W.cm^{-2}$ irradiance. All measurements are made at room temperature.*

Furthermore, the coupling between both layers still has to be revealed. We use time-resolved photoemission (TRXPS) to do so, see **Figure 2**a.[24–28] It is a pump-probe method where a fs laser is used to excite the HgTe NCs above the particle band gap, using a 1.5 eV (800 nm) photon energy. Then, the soft X-rays from the synchrotron are used to probe the energy shift of a given core level, here Hg4f (**Figure** 2b), after illumination. The sign of the shift relates to the nature of the majority carriers.[25–30] In this case, a negative shift is observed, see **Figure 2**c, meaning that holes are indeed the majority carriers,[25–30] corroborating the transport measurement (**Figure 1**c). The magnitude of the shift is a direct measurement of the film surface band bending. We notice the clear benefit of the presence of the Ag_2Te layer with an increase of the surface band bending by a factor 3 (from 15 to 50 meV): this Ag_2Te layer eases the hole extraction toward the top gold contact. The other key benefit of TRXPS comes from its unique atomic specificity enabling simultaneously the monitoring of Hg 4f state from the absorbing layer and the Ag 3d from the HTL. The two atoms have an identical relaxation decay, see Figure 2d, meaning that they are electrostatically coupled (*i.e.,* they shift rigidly together). Last, the relaxation time is around 600 ns and relates to the migration of the majority carriers (figure S9) toward the surface. This will be further discussed later.

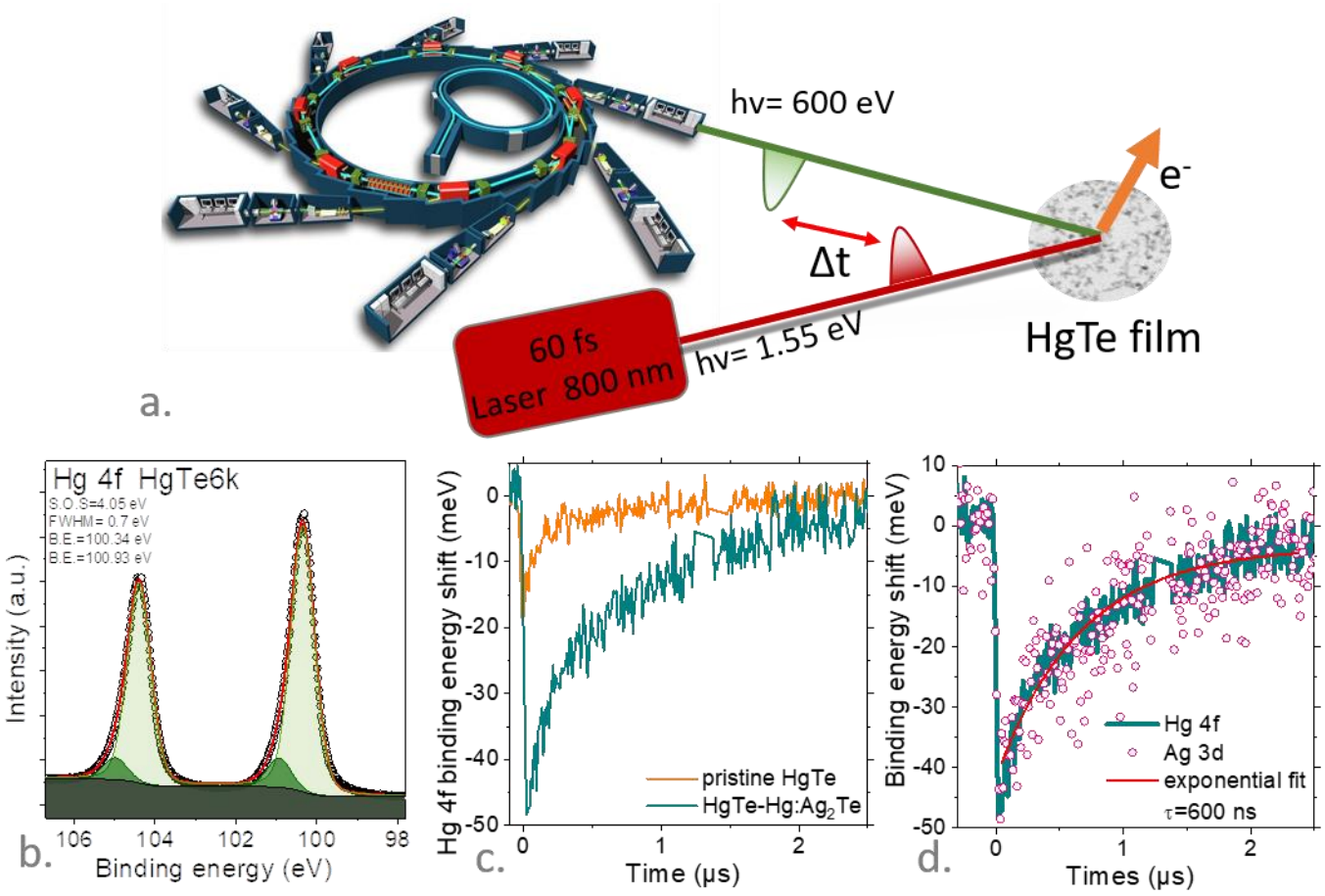

Figure 2 *a. Schematic of the pump probe photoemission. fs laser at 800 nm is used to excite the NC film and soft X-rays from synchrotron are used as a probe (hv=600 eV). b. Photoemission spectrum from the Hg 4f state. c. Binding energy of the Hg $4f_{7/2}$ state after a pulse of light (t=0) at 800 nm from a pristine HgTe NC film and from the same film covered with Hg exchanged Ag_2Te thin layer. d. Binding energy shift of the Hg $4f_{7/2}$ state and Ag $3d_{5/2}$ state after a pulse of light (t=0) at 800 nm from a HgTe NC film covered with Hg exchanged Ag_2Te thin layer. All measurements are made at room temperature, while samples are deposited on a gold substrate.*

Now that we have established that the *p*-type nature of HgTe NCs at the targeted wavelength is responsible for the limited performances, it becomes of utmost interest to couple the HgTe layer to an electron transport layer (ETL). There are a few earlier attempts in the literature to introduce an ETL coupled to HgTe absorbing NCs. Tang *et al.* have used Bi_2Se_3 nanoparticles,[13] which grow in the form of anisotropic platelets. Though the obtained performances are impressive, these platelets show poor colloidal stability, and it is difficult to obtain a pinhole-free layer from the solution. Günes *et* al[31] and Jagtap *et al.* reported the use of TiO_2 as ETL.[32] The obtained dark I-V curve is strongly rectifying thanks to the efficiency of the hole blocking layer. However, the achieved responsivity is also weak (<<mA·W^{-1}) resulting from the poor band alignment between HgTe and TiO_2. The latter layer filters not only the hole dark current but also the electron photocurrent. The material targeted to design an ETL layer coupled to an HgTe absorbing layer needs to fulfill the following requirements: (i) be *n*-type with a reasonable mobility, (ii) not absorb (or weakly) in the SWIR, (iii) present a quasi-resonant conduction band alignment with HgTe, while being strongly offset for the valence band. The latter condition requires a material with a large electron affinity. Organic materials have not been considered since, in the IR, the strong coupling to vibrations leads to fast quenching, although considerable progress has been obtained in this direction recently.[7] To remain compatible with solution processability, we have screened all III-V and II-VI materials that can be grown by colloidal synthesis. III-V materials were excluded because they tend to have lower work functions than II-VI semiconductors.[33] Previous experience with ZnO and TiO_2[17,31] excludes these candidates due to the low responsivity. Among II-VI, CdSe has the largest work function after ZnO, but its smaller band gap compared to ZnO makes it promising to achieve a deep conduction band layer. In II-VI compounds, the electron effective mass is generally weaker than the hole mass, making that confinement occurs mainly in the conduction band. Thus, to avoid generating an offset with the HgTe conduction band, we choose to grow large CdSe NCs (Figure S3) with a band edge at 640 nm. Then, to prevent this layer from becoming the bottleneck of transport, we capped the CdSe NCs with very short sulfide ligands and annealed them at 200 °C to ensure strong interparticle coupling. Finally, the *n*-type nature of such a layer has been previously established.[34] The band alignment of the CdSe/HgTe/Ag_2Te stack is determined by combining photoemission to determine the valance band and optical spectroscopy to determine the conduction band levels assuming that the coulombic corrections to the optical band gap are small, see **Figure 3**e and S5-S8. The conduction band offset between CdSe and HgTe is found to be within the XPS measurement resolution, while the valence bands present a large offset of more than 1 eV. This causes CdSe to behave as a unipolar barrier preventing any hole dark conduction. As CdSe behaves as a wide band gap material, the carrier density in this layer and the space charge region associated with the band bending propagates throughout this thin layer. We then fabricate the diode associated with the CdSe/HgTe/Ag_2Te stack, see **Figure 3**a and measure its electrical characteristic (**Figure 3**d). A TEM image of the diode shows a side view of the diode stack (**Figure 3**b). We can clearly notice an interface layer between the FTO and the HgTe. A composition profile (**Figure 3**c) extracted from Energy-dispersive X-ray spectroscopy confirms the presence of Se in this interface. The I-V curve (**Figure 3**d) appears to be more rectifying (forward bias is now 4 times larger than reverse bias under 0.1 V) than those obtained from the same device without the CdSe layer (**Figure 1**e). The 0 V dark current density has been determined to be 5×10^{-8} A·cm^{-2} at room temperature corresponding to 120 fA leakage of a 15×15 µm^2 pixel size - typical for SWIR focal plane arrays - which matches the dark current level in InGaAs sensors.

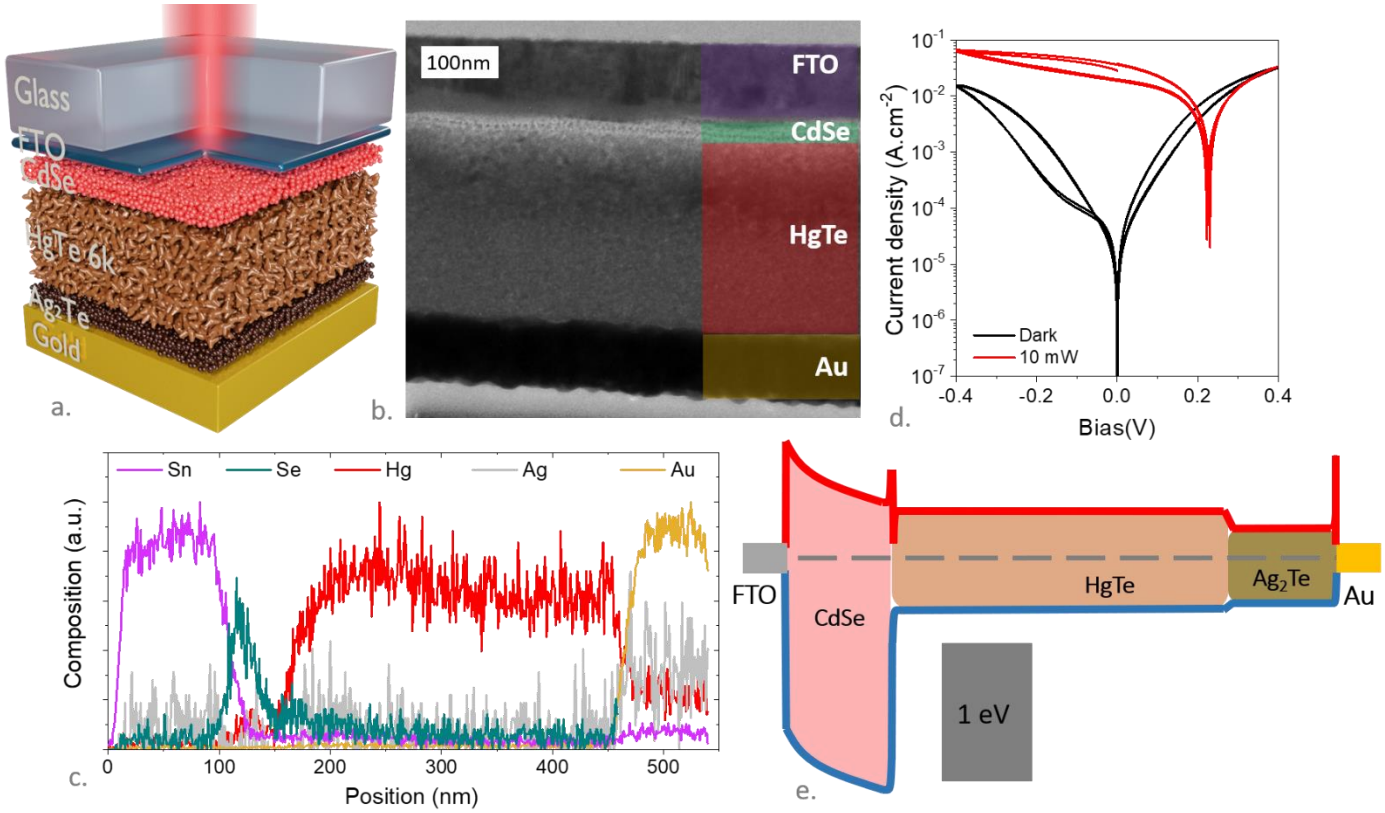

Figure 3 *a. Schematic of CdSe/HgTe/Hg:Ag_2Te photodiode used for SWIR light sensing. b. TEM image of the slice of the CdSe/HgTe/Hg:Ag_2Te diode, false colors are added to help identifying each layer. c. Composition profile extracted from energy dispersive X-ray spectroscopy obtained from the slice shown in part b. d. I-V curves for the photodiode depicted in part a under dark condition and under illumination by a 1.55 µm laser diode delivering a 0.6 W·cm^{-2} irradiance. All measurements are made at room temperature. e. Band alignment determined from photoemission for the diode depicted in part a. Also see Figure S5 to S8 for photoemission data used to determine the diagram.*

The photocurrent spectrum of the diode shows an absorption onset at 5000 cm^{-1} (2 µm), see **Figure 4**a. The responsivity of the diode under moderate irradiance (0.6 mW·cm^{-2} at 1.55 µm) reaches 0.8 A·W^{-1} for a pixel of 1 mm x 50 µm, see **Figure 4**d. For 2 µm cut-off wavelength, this responsivity corresponds to 50% external quantum efficiency. To determine the internal quantum efficiency, we have estimated the device absorption. The complex optical index of each layer is determined using broadband spectrally resolved ellipsometry, see Figure S4. These indices are then used as input for Rigorous coupled-wave analysis (RCWA) simulations to determine the absorption spectrum, absorption map, and dispersion relation. In **Figure 4**b, the absorption of the NCs (*i.e.,* without the absorption in the contacts, also see Figure S10) in the diode is given as a function of the HgTe layer thickness. In our case, the HgTe NC layer is made to be 500±50 nm, corresponding to about 50% of absorption of the incident light within the NCs. We can thus determine that the internal quantum efficiency is close to unity, thanks to the CdSe layer. To further confirm this high internal efficiency, we also have measured the reflectivity spectrum of the diode stack (see figure S12). In this diode there is no transmitted light due to the presence of the gold electrode and we can thus determine the absorption as *1-R*, with *R* the measured reflectivity. In this case we estimate the internal quantum efficiency=$\frac{resp.h.c}{\lambda e(1-R)}$ to be 93 %, with *resp* the responsivity, *h* the Planck's constant, *c* the speed of light, *e* the proton charge, $\lambda = 1.55\ \mu m$ the wavelength.

The simulation of the total absorption reveals that 10 to 15% of the incident light is lost within the metallic contacts and mainly in the FTO layer used as a partly transparent electrode, see **Figure 4**c. Certainly, the reduction of the loss in the contact will be the next challenge in this spectral range. The dispersion map (Figure S11) shows the existence of a non-dispersive resonance (*i.e.,* a Fabry-Perot resonance) for a 500 nm thick HgTe layer, which explains why the amount of absorbed light is above $1\text{-}10^{-\alpha L}$ expected for a single pass of the light through the film.

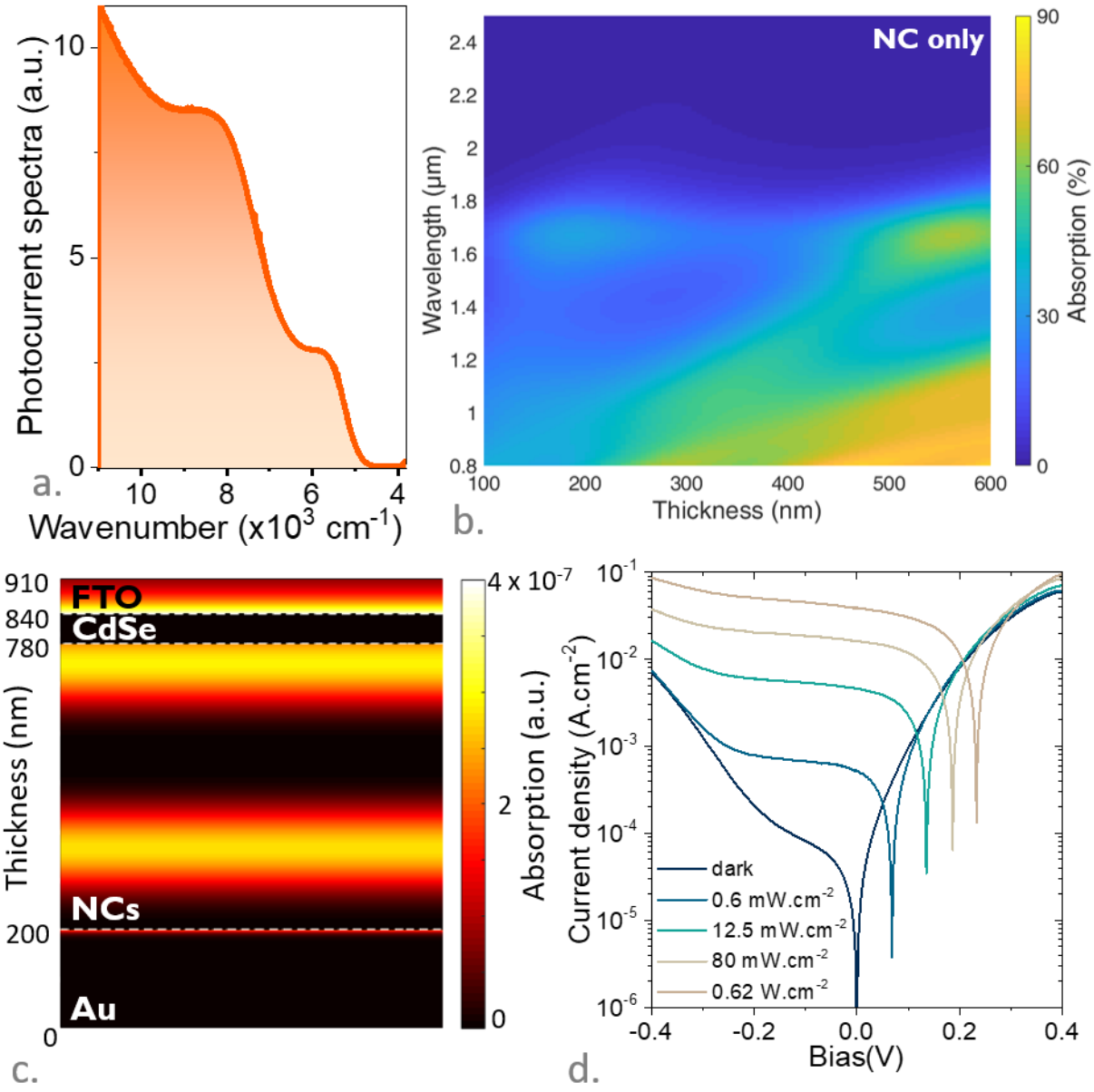

Figure 4 *a. Photocurrent spectrum of the CdSe/HgTe/Hg:Ag_2Te photodiode. b. Simulated absorption in the HgTe NCs (i.e. excluding loss in contacts) spectra as a function of the thickness of the HgTe layer in the CdSe/HgTe/Hg:Ag_2Te photodiode. c. Absorption map of the CdSe/HgTe/Hg:Ag_2Te photodiode at 1.55 µm. d. I-V curves for the CdSe/HgTe/Hg:Ag_2Te photodiode under dark condition and under illumination by a 1.55 µm laser diode delivering various irradiances.*

The specific detectivity of the diode reaches $9x10^{10}$ Jones at room temperature and $9x10^{11}$ Jones at 200 K (at 1 kHz, under null bias), see **Figure 5**a. To compare this diode performance with state-of-the-art devices, we have plotted a map of detectivity vs. responsivity (**Figure 5**b) for all devices listed in table 1 corresponding to most HgTe NC-based devices operated in the SWIR. With a detectivity almost reaching 10^{12} Jones, this device is the best performing diode reported so far based on HgTe NC operating in the same spectral range.

As expected, the time response of the device is found to be in the 200 to 700 ns range depending on pixel size[35], see **Figure 5**c. This time response is fast enough for most imaging applications and even for active imaging. This time response also matches the one revealed using TRXPS (τ=600 ns), meaning that time response is limited by the mobility of the majority carrier.

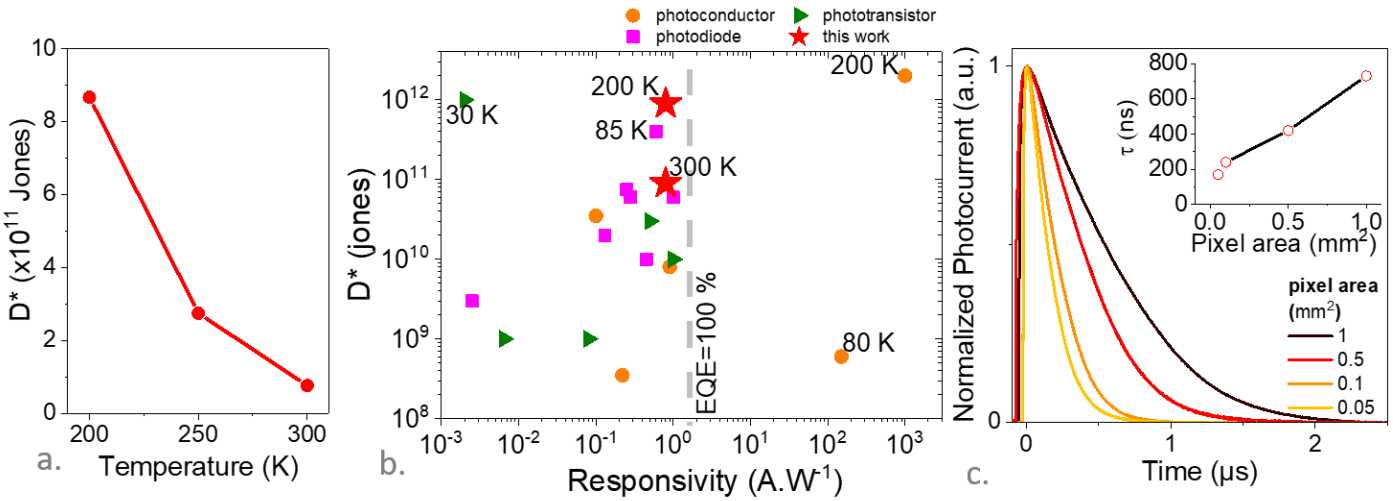

Figure 5 *a. Specific detectivity at 1.55 µm with modulation at 1 kHz for the CdSe/HgTe/Hg:Ag_2Te photodiode for two sizes of pixel as a function of the operating temperature. b. Specific detectivity as a function of device responsivity for HgTe NC-based devices operating in the SWIR, also see table S1 for associated references. c. Time response after a 1 ns pulse at 355 nm for various sizes of pixel. The inset provides the main exponential decay time as a function of pixel size.*

table 1 Figures of merit relative to light sensors operating in the SWIR and based on HgTe NCs.

Cut-off λ (µm)	**Operating mode**	**Responsivity** ($A.W^{-1}$)	**Response time**	**Detectivity** (jones)	**Operating temperature** (K)	**Specific feature**	**Ref.**
2.5	PC	0.1	10 µs	3.5×10^{10}	230	As_2S_3 surface chemistry	36
2.5	PC	1000	20 µs	2×10^{12}	200	nanotrench	15
2.5	PC	150	1.5 ms	6×10^{8}	80	HgTe decorated graphene channel	37
2.4	PC	0.9	264 µs decay time	8×10^{9}	300	Spray coating with patterning	38
2.4	PC	0.22	2.2 ms	3.5×10^{8}	300	Multicolor pixel	39
2.5	PT	6.5×10^{-3}	10 µs	10^{9}	220	Graphene electrode	8

2.5	PT	2.0 x10^{-3}	14 µs	10^{12}	30	STO gate+resonator	[40]
2	PT	<0.5	≈10 µs	3×10^{10}	300	SiO_2 back gate	[6]
2.4	PT	1	1.5 µs	10^{10}	300	Hybrid Polymer: HgTe	[7]
2.5	PT	-	15 ms	-	300	Doped-graphene/ HgTe	[41]
2.5	PT	0.08	10 µs	$>10^{8}$ $<10^{10}$	250	Planar pn junction based on dual gate	[42]
2.5	PD	2.5 x10^{-3}	370 ns	3×10^{9}	300	HgTe ink	[21]
2.5	PD	0.25	260 ns decay time	3×10^{10} (without cavity) 7.5×10^{10} (with cavity)	300	Flexible substrate	[13]
2.2	PD	1	1.4 µs decay time	6×10^{10}	300	$HgCl_2$ treatment	[19]
1.8	PD	0.13	110 ns	$2x10^{10}$	300	With resonator	[22]
2.5	PD	0.6	-	$4x10^{11}$	85	Resonator grating + fabry perot	[12]
2.4	PD	0.45	13 ns	10^{10}	300	Si/graphene/ HgTe	43
2.5	PD	0.28	2.5 µs	6×10^{10}	300	Bi_2Se_3/HgTe/ Ag_2Te	11
2	PD	0.8	170 ns	9×10^{11} 9×10^{10}	200 300	CdSe/HgTe/ Ag_2Te	**This work**

CONCLUSION

We demonstrate that CdSe NCs behave as an optimal electron transport layer once coupled to HgTe NCs with a cut-off wavelength of around 2 µm. The band alignment revealed by photoemission shows isoenergetic conduction bands and a strong offset of the valence bands, which eases photoelectron extraction while blocking the hole dark current. The obtained I-V curve is consequently more rectifying, and a low dark current density ≈5×10^{-8} A·cm^{-2} is achieved at room temperature. The device also achieves a high responsivity reaching 0.8 A·W^{-1}, corresponding to an internal efficiency above 90 % since the absorption is around 50% due to Fabry Perot resonance within the diode stack. The specific detectivity is 9×10^{10} Jones at room temperature and reaches 9×10^{11} Jones at 200 K, the highest value reported for this material in this spectral range. The diode time response can be as short as 200 ns and appears limited by band bending dynamics as revealed by time-

resolved photoemission. Future work will have to address the loss in the contact, estimated around 15 %.

ASSOCIATED CONTENT

Supporting Information include (*i*) material characterization including ellipsometry data, and photoemission measurements, (*ii*) diode fabrication procedure, (*iii*) electromagnetic simulation, (i*v*) device characterization and (*v*) comparison with state-of-the-art devices.

COMPETING INTEREST

The authors declare no competing financial interest.

ACKNOWLEDEGMENTS

The project is supported by ERC starting grant blackQD (grant n° 756225). We acknowledge the use of clean-room facilities from the “Centrale de Proximité Paris-Centre”. This work has been supported by the Region Ile-de-France in the framework of DIM Nano-K (grant dopQD). This work is supported by French state funds managed by the ANR within the Investissements d'Avenir programme under reference ANR-11-IDEX-0004-02, and more specifically within the framework of the Cluster of Excellence MATISSE and also by the grant IPER-Nano2 (ANR-18CE30-0023-01), Copin (ANR-19-CE24-0022), Frontal (ANR-19-CE09-0017), Graskop (ANR-19-CE09-0026) and NITQuantum (ANR-20-ASTR-0008-01), Bright (ANR-21-CE24-0012-02) and MixDferro (ANR-21-CE09-0029). AC thanks Agence innovation defense for PhD funding.

REFERENCES

(1) Gréboval, C.; Chu, A.; Goubet, N.; Livache, C.; Ithurria, S.; Lhuillier, E. Mercury Chalcogenide Quantum Dots: Material Perspective for Device Integration. *Chem. Rev.* **2021**, *121*, 3627–3700.

(2) Qu, J.; Rastogi, P.; Gréboval, C.; Lagarde, D.; Chu, A.; Dabard, C.; Khalili, A.; Cruguel, H.; Robert, C.; Xu, X. Z.; et al. Electroluminescence from HgTe Nanocrystals and Its Use for Active Imaging. *Nano Lett.* **2020**, *20*, 6185–6190.

(3) Qu, J.; Weis, M.; Izquierdo, E.; Mizrahi, S. G.; Chu, A.; Dabard, C.; Gréboval, C.; Bossavit, E.; Prado, Y.; Péronne, E.; et al. Electroluminescence from Nanocrystals above 2 µm. *Nat. Photonics* **2022**, *16*, 38-44.

(4) Liu, D.; Wen, S.; Guo, Y.; Yin, X.; Que, W. Synthesis of HgTe Colloidal Quantum Dots for Infrared Photodetector. *Mater. Lett.* **2021**, *291*, 129523.

(5) Ackerman, M. M.; Tang, X.; Guyot-Sionnest, P. Fast and Sensitive Colloidal Quantum Dot Mid-Wave Infrared Photodetectors. *ACS Nano* **2018**, *12*, 7264–7271.

(6) Chen, M.; Lu, H.; Abdelazim, N. M.; Zhu, Y.; Wang, Z.; Ren, W.; Kershaw, S. V.; Rogach, A. L.; Zhao, N. Mercury Telluride Quantum Dot Based Phototransistor Enabling High-Sensitivity Room-Temperature Photodetection at 2000 nm. *ACS Nano* **2017**, *11*, 5614–5622.

(7) Dong, Y.; Chen, M.; Yiu, W. K.; Zhu, Q.; Zhou, G.; Kershaw, S. V.; Ke, N.; Wong, C. P.; Rogach, A. L.; Zhao, N. Solution Processed Hybrid Polymer: HgTe Quantum Dot Phototransistor with High Sensitivity and Fast Infrared Response up to 2400 nm at Room Temperature. *Adv. Sci.* **2020**, *7*, 2000068.

(8) Noumbé, U. N.; Gréboval, C.; Livache, C.; Chu, A.; Majjad, H.; Parra López, L. E.; Mouafo, L. D. N.; Doudin, B.; Berciaud, S.; Chaste, J.; et al. Reconfigurable 2D/0D p–n Graphene/HgTe Nanocrystal Heterostructure for Infrared Detection. *ACS Nano* **2020**, *14*, 4567–4576.

(9) Buurma, C.; Pimpinella, R. E.; Ciani, A. J.; Feldman, J. S.; Grein, C. H.; Guyot-Sionnest, P. MWIR Imaging with Low Cost Colloidal Quantum Dot Films. *Proc. SPIE* **2016**, 9933, 993303

(10) Chu, A.; Martinez, B.; Ferré, S.; Noguier, V.; Gréboval, C.; Livache, C.; Qu, J.; Prado, Y.; Casaretto, N.; Goubet, N.; et al. HgTe Nanocrystals for SWIR Detection and Their Integration up to the Focal Plane Array. *ACS Appl. Mater. Interfaces* **2019**, *11*, 33116–33123.
(11) Tang, X.; Ackerman, M. M.; Chen, M.; Guyot-Sionnest, P. Dual-Band Infrared Imaging Using Stacked Colloidal Quantum Dot Photodiodes. *Nat. Photonics* **2019**, *13*, 277–282.
(12) Tang, X.; Ackerman, M. M.; Guyot-Sionnest, P. Thermal Imaging with Plasmon Resonance Enhanced HgTe Colloidal Quantum Dot Photovoltaic Devices. *ACS Nano* **2018**, *12*, 7362–7370.
(13) Tang, X.; Ackerman, M. M.; Shen, G.; Guyot-Sionnest, P. Towards Infrared Electronic Eyes: Flexible Colloidal Quantum Dot Photovoltaic Detectors Enhanced by Resonant Cavity. *Small* **2019**, *15*, 1804920.
(14) Chu, A.; Gréboval, C.; Goubet, N.; Martinez, B.; Livache, C.; Qu, J.; Rastogi, P.; Bresciani, F. A.; Prado, Y.; Suffit, S.; et al. Near Unity Absorption in Nanocrystal Based Short Wave Infrared Photodetectors Using Guided Mode Resonators. *ACS Photonics* **2019**, *6*, 2553–2561.
(15) Chu, A.; Gréboval, C.; Prado, Y.; Majjad, H.; Delerue, C.; Dayen, J.-F.; Vincent, G.; Lhuillier, E. Infrared Photoconduction at the Diffusion Length Limit in HgTe Nanocrystal Arrays. *Nat. Commun.* **2021**, *12*, 1794.
(16) Lan, X.; Chen, M.; Hudson, M. H.; Kamysbayev, V.; Wang, Y.; Guyot-Sionnest, P.; Talapin, D. V. Quantum Dot Solids Showing State-Resolved Band-like Transport. *Nat. Mater.* **2020**, *19*, 323–329.
(17) Jagtap, A.; Martinez, B.; Goubet, N.; Chu, A.; Livache, C.; Gréboval, C.; Ramade, J.; Amelot, D.; Trousset, P.; Triboulin, A.; et al. Design of a Unipolar Barrier for a Nanocrystal-Based Short-Wave Infrared Photodiode. *ACS Photonics* **2018**, *5*, 4569–4576.
(18) Gréboval, C.; Noumbé, U. N.; Chu, A.; Prado, Y.; Khalili, A.; Dabard, C.; Dang, T. H.; Colis, S.; Chaste, J.; Ouerghi, A.; et al. Gate Tunable Vertical Geometry Phototransistor Based on Infrared HgTe Nanocrystals. *Appl. Phys. Lett.* **2020**, *117*, 251104.
(19) Ackerman, M. M.; Chen, M.; Guyot-Sionnest, P. HgTe Colloidal Quantum Dot Photodiodes for Extended Short-Wave Infrared Detection. *Appl. Phys. Lett.* **2020**, *116*, 083502.
(20) Nakotte, T.; Munyan, S. G.; Murphy, J. W.; Hawks, S. A.; Kang, S.; Han, J.; Hiszpanski, A. M. Colloidal Quantum Dot Based Infrared Detectors: Extending to the Mid-Infrared and Moving from the Lab to the Field. *J. Mater. Chem. C* **2022**, *10*, 790–804.
(21) Martinez, B.; Ramade, J.; Livache, C.; Goubet, N.; Chu, A.; Gréboval, C.; Qu, J.; Watkins, W. L.; Becerra, L.; Dandeu, E.; et al. HgTe Nanocrystal Inks for Extended Short-Wave Infrared Detection. *Adv. Opt. Mater.* **2019**, *7*, 1900348.
(22) Rastogi, P.; Chu, A.; Dang, T. H.; Prado, Y.; Gréboval, C.; Qu, J.; Dabard, C.; Khalili, A.; Dandeu, E.; Fix, B.; et al. Complex Optical Index of HgTe Nanocrystal Infrared Thin Films and Its Use for Short Wave Infrared Photodiode Design. *Adv. Opt. Mater.* **2021**, *9*, 2002066.
(23) Keuleyan, S.; Lhuillier, E.; Guyot-Sionnest, P. Synthesis of Colloidal HgTe Quantum Dots for Narrow Mid-IR Emission and Detection. *J. Am. Chem. Soc.* **2011**, *133*, 16422–16424.
(24) Spencer, B. F.; Cliffe, M. J.; Graham, D. M.; Hardman, S. J. O.; Seddon, E. A.; Syres, K. L.; Thomas, A. G.; Sirotti, F.; Silly, M. G.; Akhtar, J.; et al. Chemically-Specific Time-Resolved Surface Photovoltage Spectroscopy: Carrier Dynamics at the Interface of Quantum Dots Attached to a Metal Oxide. *Surf. Sci.* **2015**, *641*, 320–325.
(25) Livache, C.; Izquierdo, E.; Martinez, B.; Dufour, M.; Pierucci, D.; Keuleyan, S.; Cruguel, H.; Becerra, L.; Fave, J. L.; Aubin, H.; et al. Charge Dynamics and Optolectronic Properties in HgTe Colloidal Quantum Wells. *Nano Lett.* **2017**, *17*, 4067–4074.
(26) Gréboval, C.; Rastogi, P.; Qu, J.; Chu, A.; Ramade, J.; Khalili, A.; Dabard, C.; Dang, T. H.; Cruguel, H.; Ouerghi, A.; et al. Time-Resolved Photoemission to Unveil Electronic Coupling between Absorbing and Transport Layers in a Quantum Dot-Based Solar Cell. *J. Phys. Chem. C* **2020**, *124*, 23400–23409.
(27) Gréboval, C.; Izquierdo, E.; Livache, C.; Martinez, B.; Dufour, M.; Goubet, N.; Moghaddam, N.; Qu, J.; Chu, A.; Ramade, J.; et al. Impact of Dimensionality and Confinement on the Electronic Properties of Mercury Chalcogenide Nanocrystals. *Nanoscale* **2019**, *11*, 3905–3915.

(28) Spencer, B. F.; Graham, D. M.; Hardman, S. J. O.; Seddon, E. A.; Cliffe, M. J.; Syres, K. L.; Thomas, A. G.; Stubbs, S. K.; Sirotti, F.; Silly, M. G.; et al. Time-Resolved Surface Photovoltage Measurements at *n*-Type Photovoltaic Surfaces: Si(111) and ZnO(1010). *Phys. Rev. B* **2013**, *88*, 195301.
(29) Amelot, D.; Rastogi, P.; Martinez, B.; Gréboval, C.; Livache, C.; Bresciani, F. A.; Qu, J.; Chu, A.; Goyal, M.; Chee, S.-S.; et al. Revealing the Band Structure of FAPI Quantum Dot Film and Its Interfaces with Electron and Hole Transport Layer Using Time Resolved Photoemission. *J. Phys. Chem. C* **2020**, *124*, 3873–3880.
(30) Bergeard, N.; Silly, M. G.; Krizmancic, D.; Chauvet, C.; Guzzo, M.; Ricaud, J. P.; Izquierdo, M.; Stebel, L.; Pittana, P.; Sergo, R.; et al. Time-Resolved Photoelectron Spectroscopy Using Synchrotron Radiation Time Structure. *J. Synchrotron Radiat.* **2011**, *18*, 245–250.
(31) Günes, S.; Neugebauer, H.; Sariciftci, N. S.; Roither, J.; Kovalenko, M.; Pillwein, G.; Heiss, W. Hybrid Solar Cells Using HgTe Nanocrystals and Nanoporous TiO_2 Electrodes. *Adv. Funct. Mater.* **2006**, *16*, 1095–1099.
(32) Jagtap, A.; Goubet, N.; Livache, C.; Chu, A.; Martinez, B.; Gréboval, C.; Qu, J.; Dandeu, E.; Becerra, L.; Witkowski, N.; et al. Short Wave Infrared Devices Based on HgTe Nanocrystals with Air Stable Performances. *J. Phys. Chem. C* **2018**, *122*, 14979–14985.
(33) Nethercot, A. H. Prediction of Fermi Energies and Photoelectric Thresholds Based on Electronegativity Concepts. *Phys. Rev. Lett.* **1974**, *33*, 1088–1091.
(34) Lhuillier, E.; Ithurria, S.; Descamps-Mandine, A.; Douillard, T.; Castaing, R.; Xu, X. Z.; Taberna, P.-L.; Simon, P.; Aubin, H.; Dubertret, B. Investigating the n- and p-Type Electrolytic Charging of Colloidal Nanoplatelets. *J. Phys. Chem. C* **2015**, *119*, 21795–21799.
(35) Vafaie, M.; Fan, J. Z.; Morteza Najarian, A.; Ouellette, O.; Sagar, L. K.; Bertens, K.; Sun, B.; García de Arquer, F. P.; Sargent, E. H. Colloidal Quantum Dot Photodetectors with 10-Ns Response Time and 80% Quantum Efficiency at 1,550 nm. *Matter* **2021**, *4*, 1042–1053.
(36) Lhuillier, E.; Keuleyan, S.; Zolotavin, P.; Guyot-Sionnest, P. Mid-Infrared HgTe/As2S3 Field Effect Transistors and Photodetectors. *Adv. Mater.* **2013**, *25*, 137–141.
(37) Grotevent, M. J.; Hail, C. U.; Yakunin, S.; Bachmann, D.; Calame, M.; Poulikakos, D.; Kovalenko, M. V.; Shorubalko, I. Colloidal HgTe Quantum Dot/Graphene Phototransistor with a Spectral Sensitivity Beyond 3 µm. *Adv. Sci.* **2021**, *8*, 2003360.
(38) Cryer, M. E.; Halpert, J. E. 300 nm Spectral Resolution in the Mid-Infrared with Robust, High Responsivity Flexible Colloidal Quantum Dot Devices at Room Temperature. *ACS Photonics* **2018**, *5*, 3009–3015.
(39) Cryer, M. E.; Browning, L. A.; Plank, N. O. V.; Halpert, J. E. Large Photogain in Multicolor Nanocrystal Photodetector Arrays Enabling Room-Temperature Detection of Targets Above 100 °C. *ACS Photonics* **2020**, *7*, 3078–3085.
(40) Gréboval, C.; Chu, A.; Magalhaes, D. V.; Ramade, J.; Qu, J.; Rastogi, P.; Khalili, A.; Chee, S.-S.; Aubin, H.; Vincent, G.; et al. Ferroelectric Gating of Narrow Band-Gap Nanocrystal Arrays with Enhanced Light–Matter Coupling. *ACS Photonics* **2021**, *8*, 259–268.
(41) Tang, X.; Lai, K. W. C. Graphene/HgTe Quantum-Dot Photodetectors with Gate-Tunable Infrared Response. *ACS Appl. Nano Mater.* **2019**, *2*, 6701–6706.
(42) Chee, S.-S.; Gréboval, C.; Magalhaes, D. V.; Ramade, J.; Chu, A.; Qu, J.; Rastogi, P.; Khalili, A.; Dang, T. H.; Dabard, C.; et al. Correlating Structure and Detection Properties in HgTe Nanocrystal Films. *Nano Lett.* **2021**, *21*, 4145–4151.
(43) Tang, X.; Chen, M.; Kamath, A.; Ackerman, M. M.; Guyot-Sionnest, P. Colloidal Quantum-Dots/Graphene/Silicon Dual-Channel Detection of Visible Light and Short-Wave Infrared. *ACS Photonics* **2020**, *7*, 1117–1121.

TOC graphic

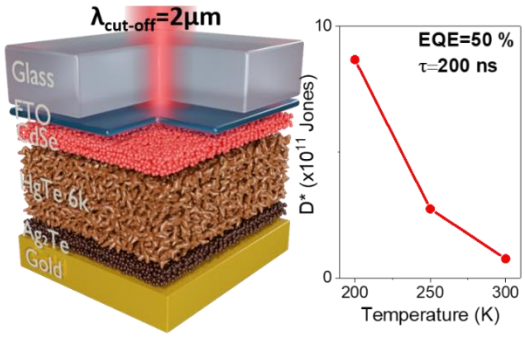
λcut-off=2µm
Glass
FTO
dSe
HgTe 6k
HgTe
Gold
EQE=50 %
τ=200 ns
D* (x10^11 Jones)
10
0
200
250
300
Temperature (K)